Millimeter-wave beam scattering by edge-plasma density fluctuations in TCV

O. Chellaï[1], S. Alberti[1], M. Baquero-Ruiz[1], I. Furno[1], T. Goodman[1], B. Labit[1], O. Maj[2], P. Ricci[1], F. Riva[1], L. Guidi[2], E. Poli[2] and the TCV team[1]

[1] *Swiss Plasma Center, École Polytechnique Fédérale de Lausanne, Lausanne, Switzerland*

[2] *Max Planck Institute for Plasma Physics, Garching, Germany*

Abstract. In magnetically confined fusion devices, the use of millimeter waves (mmw) at the electron cyclotron (EC) frequencies ranges from plasma diagnostics to plasma heating, current drive and core confinement preservation. For large tokamaks such as ITER, numerical simulations and analytical estimates suggest that plasma edge turbulence could significantly broaden the EC-beam, possibly preventing tearing modes stabilization at the designed power levels. We report measurements of mmw-beam scattering by plasma turbulence in the TCV tokamak. A mmw-Gaussian beam is injected from the top of the device and the transmitted power is measured at the bottom. We show that the measured plasma density fluctuations in the upper part of the scrape-off layer (SOL) are the cause of fluctuations of the transmitted mmw-power. A full-wave model based on COMSOL multiphysics is presented and compared against the wave-kinetic-equation solver WKBeam in a TCV case. Using the SOL turbulence simulations from the GBS code, comparison between the scattering effect on the mmw-beam with both the full-wave simulations and the experiments are ongoing. We also present experimental observations of rapid changes in the transmitted power caused by ELMs in ELMy H-mode plasma.

1. Introduction

In magnetically confined fusion devices, the use of mm-wave (mmw) beam at the electron cyclotron frequency (EC) is extensive and covers a broad range of applications. In tokamak operation, mmw-beams have become an indispensable tool for plasma heating, current drive and plasma diagnostics. A focused Gaussian mmw-beam is launched from the outside of the vessel and targets either the core or the edge of the plasma. Along its propagation, the mmw-beam traverses the outermost plasma region where it interacts with the turbulent plasma structures in the edge of the confined plasma and in the scrape-off layer (SOL). These turbulent structures are associated with density perturbations locally modifying the dielectric permittivity of the plasma and therefore affect the mmw-beam propagation. Recent studies have suggested that the beam quality (i.e. in particular its transverse width) could be deteriorated by this interaction, impacting both the current-drive localization and interpretation of the mmw-based plasma diagnostics.
In particular, concerns were raised for the upper-launcher of ITER. From the launcher to the target region in the plasma, the path length of the beam will be long enough to enable small perturbations in the SOL to cause significant changes in both the time-averaged and instantaneous beam transverse profiles, which may lead to its broadening on average [1, 2, 3, 4, 5] and consequently to a loss of efficiency in the neo-classical tearing mode stabilization [6, 7].

In this paper, we investigate the effect of the SOL turbulence and the edge-localized modes (ELMs) on the propagation of high-power mmw-beams in the Tokamak à Configuration Variable (TCV) at the Swiss Plasma Center [8]. After describing the experimental setup in section 2, we present in section 3 the numerical tools used to model mmw-wave propagation and turbulence simulations of TCV plasmas. The full-wave model based on COMSOL multiphysics is benchmarked in the case of a plasma equilibrium against the wave-kinetic-equation solver WKBeam in section 4. Experimental results show that the plasma turbulence is responsible for the instantaneous degradation of the mmw-beam profile in section 5. Using SOL turbulence simulations from the Global Braginskii Solver (GBS) [9] in section 5.2, we resolve the time-dependent profile of the mmw-beam and obtain fluctuation levels of the transmitted power of the same order as those of the experiment. Finally, in section 6 we show experimentally that in an ohmic H-mode plasma, edge localized modes have a strong effect on the mmw-wave beam propagation.

2. Experimental setup

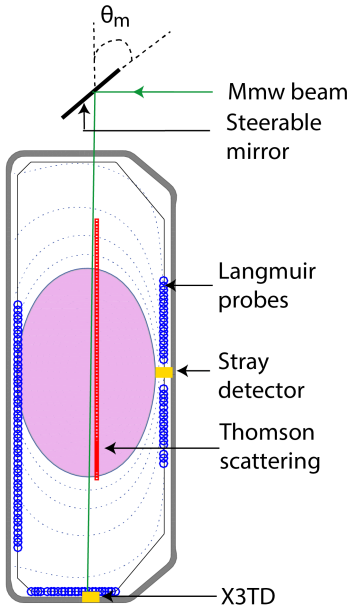

Figure 1. Experimental setup: a millimeter-wave Gaussian beam is launched in O-mode using a steerable mirror from the top of the TCV vessel (in gray). After propagating through the plasma (in purple) the beam power is detected at the floor of the vessel by the X3TD transmission diagnostic. The Thomson Scattering measurement volumes are shown by the red squares and the position of wall-mounted Langmuir probes is represented by the blue circles.

The experiments are carried out in the TCV tokamak (major radius $R_0 = 0.88\,\mathrm{m}$, minor radius $a = 0.25\,\mathrm{m}$). Amongst the main characteristics of TCV, we find its high shaping capability and its EC mmw-heating system. The shaping capability, enabled by a plasma control system made of 16 independent shaping coils, allows extreme plasma shapes. The EC system in TCV is based on second and third harmonic X-mode heating at 82.4 GHz and 117.8 GHz, respectively [10], and can inject up to a total power of 4.5 MW. Using a universal polarizer O-mode is also possible. The path length of the X3 beam to the X3 transmission diagnostic in TCV is about 1.7 m (see below) which is comparable to the path length of the edge-to-resonance path in ITER [11].

In ITER, the upper launcher will inject a beam in the ordinary mode [11]. Plasma dielectric properties for the mmw in O-mode depend only on the plasma density and not on magnetic field. To mimic the ITER upper launcher scheme, the third harmonic beam in TCV (100 kW) is launched in the O-mode from the top of the vessel using a steerable mirror, as schematically shown in fig. 1. After propagation through the plasma, the transmitted power reaching the floor of the vessel

is coupled to the X3TD diagnostic [12], oriented in the O-mode for the purpose of these experiments. An hexagonal array of 241 circular holes with diameter $d = 1.2$ mm, (cut-off frequency of the lowest order (TE_{11}) circular mode is $f_c = 146.4\,\mathrm{GHz}$), acts as a $-55\,\mathrm{dB}$ attenuator. The mmw-power is then coupled to a $WR6.5$ rectangular waveguide through a lens horn antenna and measured by a Schottky diode. Since the X3TD diagnostic is fixed at a fixed radial position $R = 0.88\,\mathrm{m}$, the poloidal angle of the mirror is swept in order to reconstruct the beam profile at the floor of the vessel. For cases where the beam is distorted by the refraction from the plasma, like the ones studied in this paper, a comparison with a mmw-propagation code is needed to perform the reconstruction. More details on the mmw-setup can be found in [10, 12]. The stray radiation detector consists of a Schottky diode attached to an open fundamental-mode rectangular waveguide, and installed on the equatorial mid-plane of the vessel, on the same sector as X3TD. The stray radiation detector was originally installed to protect the vessel windows from non-absorbed mmw-power. Here, it is used as a qualitative detection of power redistribution linked to the plasmas dynamics.
The plasma equilibrium is reconstructed using the LIUQE equilibrium reconstruction code [13]. The electron density and temperature profiles are obtained from Thomson Scattering (TS) data [14] with a vertical spatial resolution of 6 mm, as shown in fig. 1.

A set of 114 wall embedded Langmuir probes (LPs) are installed in the TCV vessel [15]. Their position in the poloidal plane is shown in fig. 1. The LPs, biased at -100 V, are operating in the ion saturation regime. In this regime, the ion saturation current is linked to the electron density n_e via the Bohm condition: $I_{sat} = n_e c_s A$, where c_s is the ion sound speed and A the effective surface of the probe [15].

3. Numerical tools for millimeter wave propagation and turbulence simulations in TCV

In this section, we first describe the numerical tools used in this paper. Then we introduce first the beam propagation models, i.e. the COMSOL-based full-wave model and the WKBeam code. Their results are compared in a TCV case. Finally, we present the Global Braginskii Solver for turbulence simulations.

3.1. The full-wave model

The propagation of mmw in magnetized plasmas is typically modeled in the high-frequency/short-wavelength approximation [16, 17] where ray or beam tracing codes provide mmw-wave beam evolution in an inhomogeneous plasma. For inhomogeneities in the plasma with typical scale L_c and wavelength λ of the mmw such that $\lambda/L_c \sim 1$, this approximation is no longer valid and a more recent generalization of this approach [18, 19] or a full-wave model is needed to simulate the propagation of the mmw-beam [3, 2]. Therefore, to account for the SOL turbulence effect on the mmw beam, we have implemented a 2D full-wave numerical model based on the finite element solver COMSOL [20]. The mmw-beam transverse profile in the poloidal plane is calculated by solving the full-wave equation 1, and considering the plasma dielectric properties based on a cold plasma model. We consider the plasma as stationary at a given time τ [21] and thus reduce the cold plasma model to a single vector equation for the electric field $\mathbf{E}(\mathbf{x},\omega,\tau)$, where $\mathbf{x}$ is the position vector and ω the pulsation of the mmw, in frequency domain, namely,

$$\nabla\times\big(\nabla\times\mathbf{E}(\mathbf{x},\omega,\tau)\big)+\frac{\omega^2}{c^2}\hat{\epsilon}_r(\mathbf{x},\omega,\tau)\mathbf{E}(\mathbf{x},\omega,\tau)=\mathbf{S}(\mathbf{x},\omega), \quad (1)$$

where c is the speed of light in free space, and $\hat{\epsilon}_r(\mathbf{x},\omega)$ is the cold plasma dielectric tensor [22] computed with the equilibrium magnetic field and with density $n_e(\mathbf{x},\tau)$ frozen at time τ. The source $\mathbf{S}$ accounts for the Gaussian beam launched at the mirror position with the polarization chosen in order to excite the O-mode. Differently from the standard derivation which relies on the properties of the Stix reference frame [23], here we make no assumption on the orientation of the magnetic field. The resulting expression for the dielectric tensor can be readily evaluated given the components of the magnetic field and the density profile in an arbitrary Cartesian coordinate system. One can show that in an arbitrary Cartesian coordinate system $\mathbf{x} = (x_1, x_2, x_3)$, the dielectric tensor can be written as:

$$\epsilon_r = \begin{pmatrix} Sa_1 + Pb_1^2 & +iDb_3 + Qb_1b_2 & -iDb_2 + Qb_1b_3 \\ -iDb_3 + Qb_2b_1 & Sa_2 + Pb_2^2 & +iDb_1 + Qb_2b_3 \\ +iDb_2 + Qb_3b_1 & -iDb_1 + Qb_3b_2 & Sa_3 + Pb_3^2 \end{pmatrix}$$

with $\mathbf{b}(\mathbf{x}) = [b_1(\mathbf{x}), b_2(\mathbf{x}), b_3(\mathbf{x})]$ the unit vector of the magnetic field defined as $\mathbf{b}(\mathbf{x}) = \frac{\mathbf{B}(\mathbf{x})}{|\mathbf{B}(\mathbf{x})|}$, $\mathbf{B}(\mathbf{x})$ being the magnetic field vector and $a_i = 1 - b_i^2$ with $i = 1, 2, 3$. S, D and P are the standard Stix parameters as defined in [23] and $Q = P - S$. Equation (1) is solved for a sequence of points in time τ_i with $\Delta\tau = \tau_{i+1} - \tau_i = 4\,\mu\mathrm{s} \gg 2\pi/\omega$, thus obtaining a sequence of beams $\mathbf{E}_i(\mathbf{x},\omega)$ corresponding to different density snapshots. The time-resolved 2D profiles of the electron density $\tilde{n}_e(\mathbf{x},\tau_i)$ are calculated by a superposition of the GBS simulations of the SOL to the experimental electron density profile obtained from the Thomson Scattering diagnostic, i.e. $\tilde{n}_e(\mathbf{x},\tau_i) = \underbrace{n_{e0}(\mathbf{x})}_{\text{TS}} + \underbrace{\delta\tilde{n}_e(\mathbf{x},\tau_i)}_{\text{GBS}}$. More details are given in section 3.3. The spatial mesh size l used in COMSOL is smaller than $\lambda/5$ and $l/L_c \ll 1$.

Absorbing boundary conditions [20] are used at the edge of the computational domain.

3.2. The WKBeam code

The WKBeam code [18] is based on the statistical description of waves in random media initially put forward by Karal and Keller [24] and later developed by McDonald [25]. In this approach the plasma with time-dependent turbulent fluctuations is modeled as an ensemble of time-independent random perturbations of the plasma equilibrium. The main quantity computed by the code is the average electric-field energy density in the $(\mathbf{x}, \mathbf{N})$ phase space, which is mathematically defined as the ensemble-averaged Wigner function $w_\alpha = w_\alpha(\mathbf{x}, \mathbf{N})$ for the wave electric field. Here the index α labels cold-plasma wave modes (either $\alpha = \mathrm{O}$ for the ordinary mode or $\alpha = \mathrm{X}$ for the extra-ordinary mode), $\mathbf{x}$ is the position in the three-dimensional physical space, and $\mathbf{N}$ the refractive index vector of the wave. The relevant equation for w_α has the form of a constrained kinetic equation in the $(\mathbf{x}, \mathbf{N})$ phase space, namely the wave kinetic equation, which is solved by a Monte Carlo method. Having computed the quantity w_α, post-processing tools allow us to obtain information on the transport of the wave energy as well as power deposition in the plasma, averaged over a time interval longer than the turbulence correlation time.

The physics justification of this statistical approach relies on two main assumptions: (1) there is a scale separation between the transit time of the wave in the plasma and the typical time-scale of the turbulent fluctuations, i.e., turbulence can be considered "frozen" for the beam propagation; (2) the amplitude of the fluctuations is such that the Born scattering approximation applies.

The Wigner function w_α is computed in the semi-classical (short wave-length) limit $\lambda/L \ll 1$, where L is the typical spatial scale of the plasma *equilibrium* (typically of the order of the plasma minor radius). An important consequence of the statistical approach is that the validity of the theory is controlled by the scale L of the equilibrium, and not that of the turbulence ($L_c \ll L$), thus allowing for arbitrary short-scale fluctuations (differently from a brute-force WKB approach).

Mode conversion due to the merging of dispersion surfaces in the vacuum region and cross-scattering polarisation are neglected in this study.

In the following, the WKBeam is used in the case of a plasma with no turbulence to perform the benchmark of the COMSOL full-wave model. Studies are in progress to treat the propagation of mmw-beams in the TCV turbulence based on the statistical properties of the GBS simulations.

3.3. The GBS code

The GBS code [26, 27] was developed in the recent years to simulate plasma turbulence in the open field line regions of tokamaks [28, 29] and basic plasma physics devices [9]. Given its high collisionality, the SOL is typically studied using a plasma fluid description such as the Braginskii fluid approximation. Since turbulence time scales in the SOL are much slower than the ion cyclotron time and the scale lengths perpendicular to the magnetic field are longer than the ion Larmor radius, Braginskii's equations are typically simplified by using the drift approximation. A complete description of the equations and solving scheme for the GBS code can be found in [29]. For the present study, we make use of the infinite aspect ratio of the tokamak ($R_0/a \gg 1$), cold ions assumptions and ignore the neutral dynamics. We take into account the plasma elongation following the results in [30].
The GBS simulations being performed in the normalized units $\theta = \log(\frac{n_e}{n_{e,LCFS}})$ the coefficient factor $n_{e,LCFS}$ is chosen to match the experimental Thomson data. A rigorous validation of the simulations against the experiments is presented in [31] and shows that the fluctuation level is about twice smaller in GBS compared to the experiments, we therefore use $\delta n_{e,COMSOL}(\mathbf{x}, \tau_i) = 2\delta n_{e,GBS}(\mathbf{x}, \tau_i)$

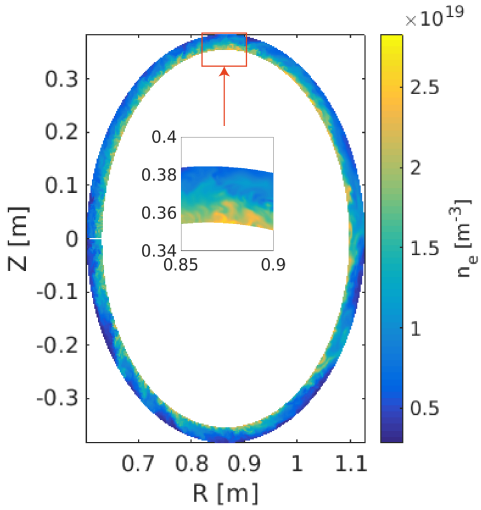

Figure 2. Poloidal snapshot of the electron density associated with the SOL turbulence computed from GBS. The electron density of the confined plasma (i.e. inside the ellipse) is given by TS data.

Figure 2 shows a snapshot of a poloidal section of the electron density in the SOL corresponding to the L-mode plasma of the experiments described in the following. We remark the presence of structures elongated along the field lines and *red* which are typically referred to as blobs. The blobs are generated in the neighborhood of the last closed flux surface and

propagate radially outwards towards the low field side [28]. They are responsible for local increases of the electron density and thus a decrease of the dielectric permittivity.

4. First comparison of the COMSOL model and WKBeam in a TCV case

The mmw beam at the mirror is described by a Gaussian beam with a half width at 1/e of the electric field amplitude $w = 39\,\text{mm}$ and a curvature radius of the phase front $R_b = -98\,\text{cm}$. The mirror is such that the beam is focusing in the poloidal plane. The beam is injected at $R = 86$ cm with a poloidal angle of $\theta_m = 44.45°$. Radial profiles of the normalized square of the electric field amplitude $\frac{|E(R,z_0)|^2}{\int_{-\infty}^{+\infty}|E(R,z_0)|^2 \mathrm{d}R}$, at the location of the launching mirror ($z_0 = 98.85\,\text{cm}$) and the detector ($z_0 = -77\,\text{cm}$) are shown in fig. 3a).

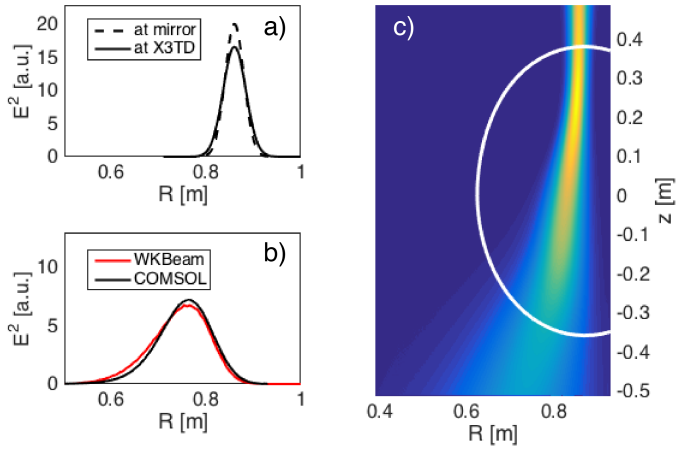

Figure 3. a) Electric field amplitude profiles before ($z = 0.99\,\text{m}$) and after ($z = -0.77\text{m}$) propagation in vacuum, at the location of the X3TD detector computed using the full-wave model based on COMSOL. The profiles are normalized using the L_1 norm. b) Electric field amplitude profile et $z = -40\,\text{cm}$, after propagation in the plasma (O-mode) and comparison with the WKBeam code. c) 2D section of the electric field associated with the mmw beam propagating through the L-mode plasma. The last closed flux surface is represented by the white contour.

As a first step, the two codes are compared for the beam propagation in vacuum. WKBeam being a 3-D model, the profile is obtained by integrating the beam profile in the direction perpendicular to the poloidal plane of COMSOL. Both codes are found in agreement with the analytic form of a Gaussian beam propagating in vacuum. Both codes are then compared in the case of the beam propagating in a quiescent plasma (fig. 3 b,c). The reconstructed magnetic equilibrium of the L-mode plasma shown in fig. 4 is used to compute the dielectric tensor of the plasma, which is then used as an input to the COMSOL code. The beam cross-section in fig. 3c shows that the beam is refracted towards the high field side, resulting in a radial displacement of the beam and its broadening. A radial profile of $|E(R,z)|^2$ at the output of the plasma ($z = -40\,\text{cm}$) is shown in fig. 3b and is compared to the profile obtained using the WKBeam code. To quantify the agreement between the two profiles, we define the parameter:

$$\zeta = \frac{|\int_{R_1}^{R_2} \mathbf{E_C}(Z,R)\cdot\mathbf{E_W}(Z,R)\mathrm{d}R|}{\sqrt{\int_{R_1}^{R_2}|\mathbf{E_C}|^2\mathrm{d}R\int_{R_1}^{R_1}|\mathbf{E_W}|^2\mathrm{d}R}} \quad (2)$$

Where $\mathbf{E_C}$ is the electric field computed by the COMSOL-base model and $\mathbf{E_W}$ the electric field computed by the WKBeam model. R_1 and R_2 are the limits of the computational domain at the corresponding Z position. The parameter ζ is equal to 0 for two distinct electric field profiles and it is equal to 1 for identical profiles. We find $\zeta = 0.99$, which shows a good agreement between the two models. The inspection of fig. 3b), shows a slight difference in the position of the maximum of the electric field profile and in the tails. Both could be associated with a difference in the interpolation of the equilibrium profiles computed by the two codes.

5. Identifying the SOL turbulence effect on mmw-beam

In this section, we present experimental measurements of the transmitted mmw-power in the case of an elongated L-mode plasma. We show that fluctuations of the electron density in the SOL are responsible for fluctuations in the transmitted mmw-power. Finally, using turbulence simulations from the GBS code, we compute the instantaneous profile of the mmw-beam using the COMSOL full-wave model.

5.1. Experimental observations

Discharge *60612* features an elongated ($\kappa = 1.52$) L-mode deuterium plasma, located at $z = 0$ cm with central density $n_e(0) = 7.3\times10^{19}\ \text{m}^{-3}$, $T_e(0) = 0.8\,\text{keV}$ and $B_T = 1.40\,\text{T}$ on axis. The time-averaged profiles of the electron density from Thomson Scattering measurements is shown in fig. 4b). At this density, the cut-off frequency for the O-mode is at 76.7 GHz, therefore no reflection of the beam from the cut-off is expected. The absorption of the mmw is also expected to be negligible. In the experiments, no increase of T_e associated with the injection of the mmw-power is observed. During the discharge, fluctuations of the I_{sat} measured by the Langmuir probes are observed, as shown in fig. 4c. Positive bursts in the signal are associated with the presence of blobs in the SOL.

During the current flat-top, the mmw-beam is swept across the detector by varying the angle of the

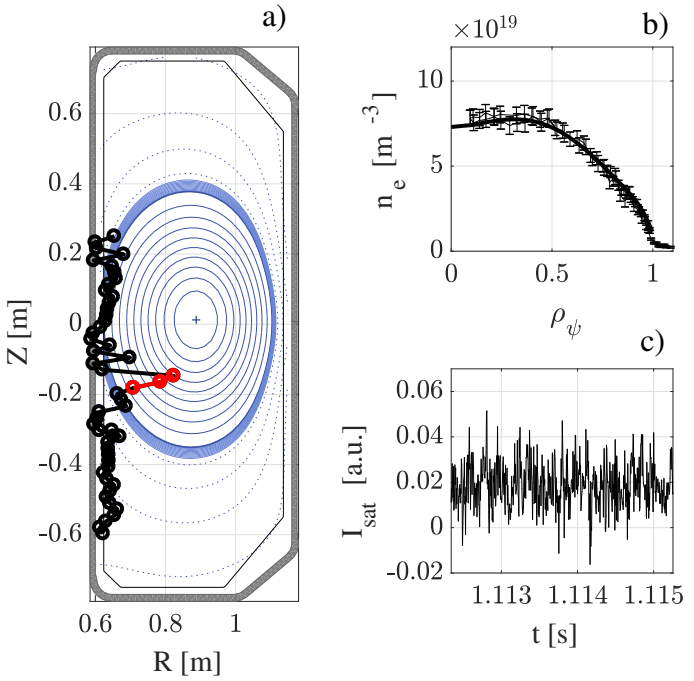

Figure 4. Limited L-mode plasma: a) flux contours of the magnetic equilibrium of the plasma. Correlation level between the LP I_{sat} signal and the transmitted mmw-power. b) Fit of the electron density and temperature profiles from the TS diagnostic. c) ion saturation current measured by the Langmuir probe in the inner wall associated with the maximum level of correlation in a).

poloidal mirror from $\theta_m = 44°$ to $\theta_m = 46°$. The detected power signal, fig. 5a), is characterized by the presence of fluctuations which are not present when the beam is swept in vacuum. We define the fluctuation level Σ, by $\Sigma = \sigma(P)/\langle P\rangle$ where σ is the standard deviation and $\langle P\rangle$ the time-averaged value of the transmitted power. In the absence of a plasma, the gyrotron power is pulsed, with a pulse duration of 8 ms, to avoid damage in the vessel. Σ is computed for each pulse an we find a fluctuation level in vacuum $\Sigma \leq 0.1$. Both $\langle P\rangle$ and Σ in the presence of a plasma are shown in fig. 5b,c), respectively. The two quantities are estimated from a set of $N = 400$ independent measurements, i.e. separated by a time delay larger than the autocorrelation time of P, in this case $\approx 50\mu s$. The errors shown in fig. 5 result from the statistical errors in the estimates [32, 33]. In this case, the fluctuation level is higher and ranges from $\Sigma = 0.2$ at the maximum of transmitted mmw-power to $\Sigma = 0.5$ around the minimum of transmitted mmw-power.

To investigate the origin of the fluctuations in the signal, we compute the cross-correlation [21] between the detected power signal and the I_{sat} signal from the wall embedded LPs [15]. Figure 4a) shows the maximum cross-correlation coefficient obtained for the signal of each probe. The probe associated with the maximum level of cross-correlation lies on a field line which intersects the path of the beam at the location of the upper-part of the scrape-off layer, at $Z = 0.41$ m and $R = 0.89$ m. The corresponding maximum correlation coefficient is $|C_{max}| = 0.16 \pm 0.02$ [34]. The probes associated with a level of correlation lower than $|C_{max}| = 0.08 \pm 0.02$ (in black in fig. 4a) do not lie on field lines intersecting the path of the beam as opposed to those associated with $|C_{max}| \geq 0.08$ (in red in fig. 4a). This suggests that the SOL has an effect on the fluctuation of the transmitted mmw-power and should be taken into account in the mmw-simulations. This effect is investigated in more details in section 5.2.

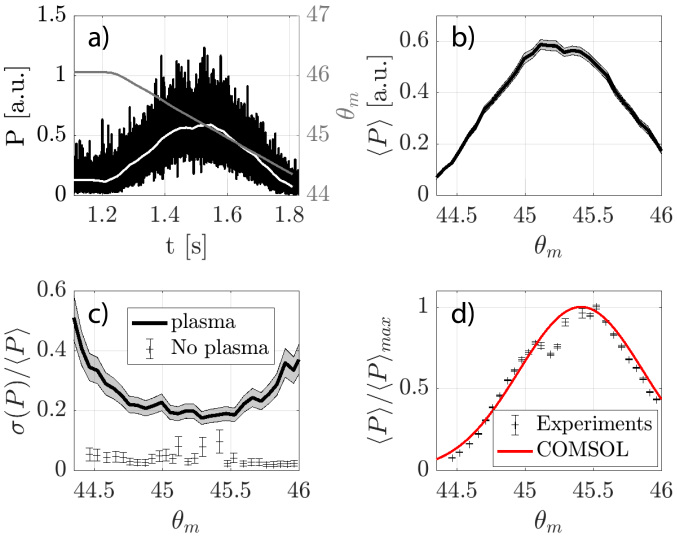

Figure 5. a) Detected mmw-power during a scan in the poloidal angle θ_m of the injection mirror. The transmitted power averaged over time windows of 20 ms is shown in white. b) transmitted power averaged over time-windows of 20 ms as a function of θ_m. c) normalized standard-deviation of the transmitted signal computed over time-windows of 20 ms as a function of θ_m. d) Black crosses: Detected power in vacuum as a function of θ_m normalized to its maximum value.Gray areas in b,d) indicate the statistical error of the estimates [33, 32]

.

5.2. Simulating the instantaneous profile of the mmw-beam

We investigate the effect of the edge-localized density fluctuations on the propagation the beam propagation using full-wave simulations, as described in section 3.1. We define a synthetic diagnostic for the power measurement of X3TD by $P_{syn} = \frac{1}{d_{diag}} \int_{X3TD} |E|^2 G(R) dR$, where $G(R)$ is the transfer function of X3TD and d_{diag} the diameter of the HE_{11} waveguide. We suppose that all the power going through the HE_{11} waveguide is measured by the schottky diode and therefore we consider that X3TD can be modeled by an attenuating

cap placed on top of an HE_{11} waveguide of diameter $d_{diag} = 63mm$. The best-fit gaussian profile for the HE_{11} mode of the waveguide, which has a diameter $d_{diag} = 63$ mm, is $e^{-\frac{(R-R0)^2}{0.02}}$ where R and R_0 are in m. We thus use $G(R) = Ae^{-\frac{(R-R0)^2}{0.02}}$, where A is a coefficient of attenuation. The comparison for the scan of the θ_m in vacuum from both the full-wave simulations and the experiments are shown in fig. 5d). An offset of 0.39deg in the experimental θ_m has been taken into account. Fig. 5d) shows a good agreement between the experimental and numerical profiles. Around 45.2 deg, the experimentally measured transmitted power is lower than the one from the simulations. At those injection angles, part of the reflected power goes into the transmission lines of the gyrotron and disturbs their operation.

The 2D electron density fluctuation profiles from GBS for the elongated plasma (discharge *55394* in [31]) are superimposed on the 2D plasma equilibrium. A snapshot of the electron density associated with the SOL turbulence from GBS is shown in fig. 2.The injection is performed at $R = 0.88$ m and $\theta_m = 45.3°$. The poloidal angle of the mirror is taken where the maximum in the transmitted mmw-power has been measured. The magnetic field is taken to be unperturbed by the presence of the SOL. Figure 6 compares the mmw-wave electric-field amplitude profiles, at the $z = -0.77$ m location of the transmission diagnostic, after propagation in the plasma and through the electron density fluctuations in the SOL. The turbulence in the SOL is responsible for strong time-dependent spatial fluctuations of the mmw-beam profile.

We find a normalized level of fluctuations $\Sigma_{syn} = \sigma(P_{syn})/\langle P_{syn}\rangle = 0.16 \pm 0.03$ comparable to the experimental level of $\Sigma = 0.2$ where N is the number of snapshots of the electron density used in the simulations. Since N is not sufficiently large to accurately characterize the distribution of P_{syn}, the values of $P_{syn}/\langle P_{syn}\rangle$ computed for each snapshot are shown in fig. 6. Figure 6 shows that instantaneously, the measured power P_{syn} may vary up to 40% of its average value. The analysis is still not conclusive but suggests that the observed fluctuations in the transmission signal can be associated, at least partially, with the scattering of the mmw-beam from the SOL turbulence. A rigorous comparison of the moments of the distribution would require a large number of samples (i.e. $N \geq 1000$). The numerical analysis is ongoing but the numerical efforts are outside the allocated time for this publication.

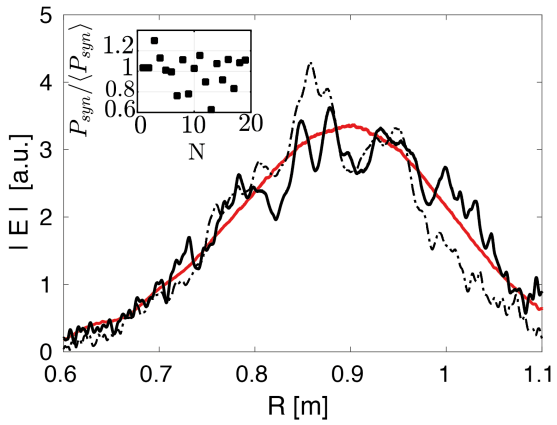

Figure 6. Profile of the mmw amplitude of the electric field at the z-location of the mmw-transmission detector obtained using the full-wave simulations. The red curve is computed with the plasma equilibrium and the two black curves correspond respectively to the perturbed mmw-beam associated with two different snapshots of the GBS turbulence. The insert shows the power P_{syn} coupled to the detector for each one of the $N = 20$ snapshots.

6. Effect of the ELMs on the mmw-beam

In this section, after presenting an ELMy H-mode scenario in TCV, we will show experimentally that the ELMs affect the mmw-power transmission.

6.1. Experimental observations

Discharge *60762* is an H-mode deuterium plasma localized at $z = 23$ cm. The electron density and temperature on axis are respectively $n_e = 6.1 \times 10^{19} m^{-3}$ (fig. 7b) and $T_e = 1.1$ keV, and the toroidal magnetic field is $B_T = 1.41$ T. In the H-mode phase, the plasma is characterized by the presence of ELMs, which are detected as bursts in the H_α signal, as shown in fig. 7c). The typical timescale of an ELM event is ≈ 3 ms.

The mmw beam is injected at $R = 88$ cm, with a poloidal angle $\theta_m = 46.4°$. The detected power is shown in fig. 8a), and reveals drops in the detected power synchronized with the ELMs detected by the vertical H_α photodiode. Fig. 8a) shows that the detected power drops to a level close to zero when the H_α signal is maximum. The average effect of ELMs on the detected mmw-power is obtained by performing conditional sampling (CS) [35] of the mmw-power signal and the H_α signal over many ELM events with a time window centered around each ELM event. All CS quantities are labeled with a $\sim$ except for τ. The relative time $\tau = 0$ ms corresponds to the detection of the ELMs. Fig. 8c) shows the result of CS of the H_α signal. It is characterized by a phase of fast increase of the signal, corresponding to the crash of the ELM,

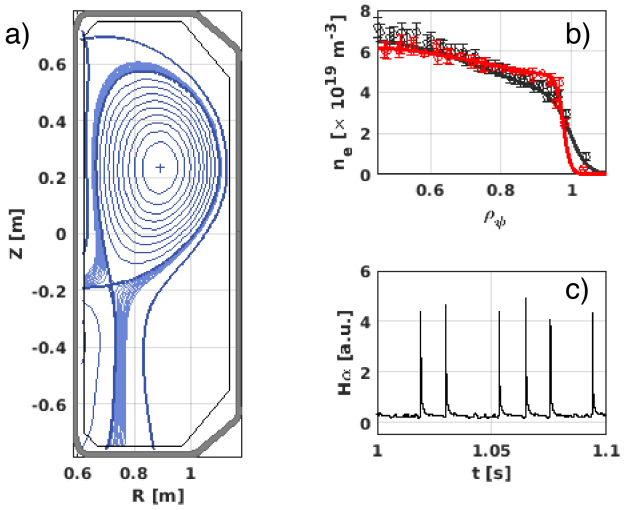

Figure 7. ELMy ohmic H-mode plasma: a) flux contours of t plasma b) Electron density profiles from the TS diagnostic befc the ELM (black) and after (red). c) ELM events are associat with bursts in the H_α signal.

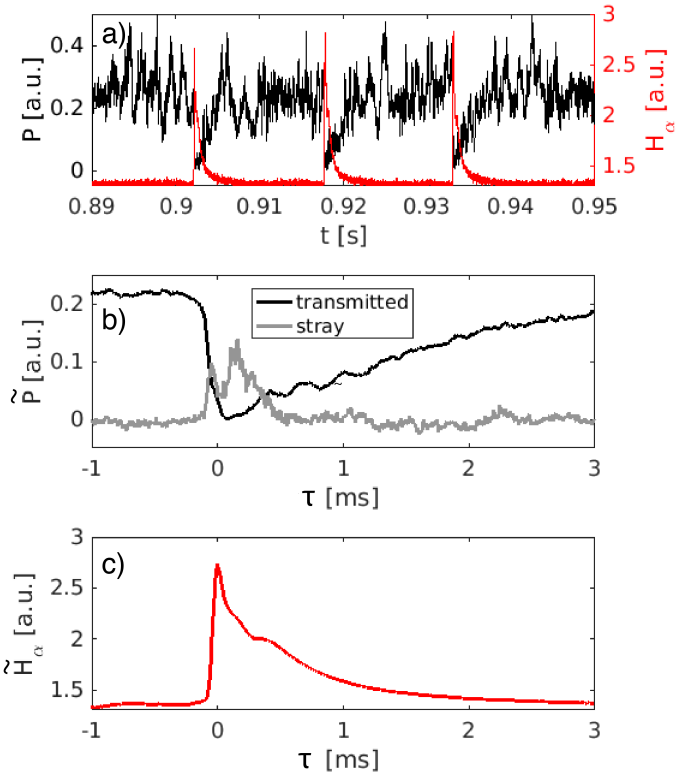

Figure 8. a) Detected mmw-power signal and $H\alpha$ signal. The bursts in the $H\alpha$ are associated with the ELMs. b) Conditional sampling (CS) of the detected mmw-power signal and the stray signal averaged over many ELM events. c) Conditional sampling (CS) of the $H\alpha$ signal.

which lasts ≈ 0.1 ms, followed by a slower phase of d cay lasting ≈ 2 ms. The results of CS of the detecte mmw-power over $N \approx 200$ events are presented in fi 8b). The detected mmw-power exhibits a fast decrea during the first phase of the ELM and recovers its ir tial value in a time scale of ≈ 3 ms. The results of the CS of the stray detector show an increase of the stray power during the first 0.5 ms after the ELM crash. This means that during the ELM event, part of the mmw-power is directed towards the low-field side of the vessel.

This study shows that the ELM is responsible for a substantial perturbation of the mmw-beam propagation and could be caused by a redistribution of the electron density during the ELM. Investigations are ongoing on TCV to understand the underlying mechanisms.

7. Conclusions

In this paper, we have shown a successful benchmark between a full-wave model implemented in COMSOL Multiphysics and the WKBeam code for the beam propagation in a quiet plasma. Combining unique experimental observations and numerical simulations, we have shown that the plasma is responsible for instantaneous fluctuations of the transmitted mmw-power. The fluctuations of the transmitted mmw-beam power are higher than 0.2 of the average transmitted mmw-beam power. The mmw-beam propagation in the transient plasma profile, affected by the fluctuations of the electron density in the SOL, has been computed using the turbulence code GBS and the full-wave model. The results show how the turbulence in the SOL affects the beam propagation, inducing fluctuations of the transmitted power with levels consistent with the experiments. These results also suggest that unlike in the DIII-D, where a broadening of the EC-power deposition was recently observed [36], the mmw-beam in TCV might not suffer from a strong broadening caused by the SOL. A precise knowledge of the turbulence parameters (i.e electron density fluctuation level, scale length of the turbulent structures and width of the turbulent layer) in ITER is still needed to enable quantitative predictions of effect of the SOL on the upper-launcher mmw-beam propagation. Finally, we have shown experimentally that ELMs cause a rapid change in the mmw-beam propagation in the plasma. Further analyses are ongoing to disentangle the underlying mechanisms.

This work has been carried out within the framework of the EUROfusion Consortium and has received

funding from the Euratom research and training programme 2014-2018 under grant agreement No 633053. The views and opinions expressed herein do not necessarily reflect those of the European Commission.This work was supported in part by the Swiss National Science Foundation. Part of the simulations presented herein were carried out on the CINECA Marconi supercomputer within the framework of the GBSSOL project.

[1] C. Tsironis, A. G. Peeters, H. Isliker, D. Strintzi, I. Chatziantonaki, and L. Vlahos *Phys. Plasmas*, vol. **16**, p. 112510, 2009.

[2] A. Köhn, E. Holzhauer, J. Leddy, M. B. Thomas, and R. G. Vann *Plasma Phys. Control. Fusion*, vol. **58**, p. 105008, 2016.

[3] A. K. Ram, K. Hizanidis, and Y. Kominis *Phys. Plasmas*, vol. **20**, p. 056110, 2013.

[4] A. Snicker, E. Poli, O. Maj, L. Guidi, A. Koehn, H. Weber, G. D. Conway, M. A. Henderson, and G. Saibene *Nucl. Fusion*, vol. **58**, p. 016002, 2017.

[5] M. W. Brookman, M. E. Austin, K. W. Gentle, C. C. Petty, D. E. Ernst, Y. Peysson, J. Decker, and K. Barada *EPJ Web of Conferences*, vol. **147**, p. 03001, 2017.

[6] E. Poli *et al. Nucl. Fusion*, vol. **55**, p. 013023, 2015.

[7] Y. Peysson, J. Decker, L. Morini, and S. Coda *Plasma Phys. Control. Fusion*, vol. **53**, p. 124028, 2011.

[8] S. Coda, J. Ahn, R. Albanese, S. Alberti, E. Alessi, S. Allan, H. Anand, G. Anastassiou, Y. Andrèbe, C. Angioni, *et al. Nuclear Fusion*, vol. 57, no. 10, p. 102011, 2017.

[9] P. Ricci, C. Theiler, A. Fasoli, I. Furno, K. Gustafson, D. Iraji, and J. Loizu *Physics of Plasmas*, vol. 18, no. 3, p. 032109, 2011.

[10] S. Alberti, G. Arnoux, L. Porte, J.-P. Hogge, B. Marletaz, P. Marmillod, Y. Martin, S. Nowak, and T. Team *Nuclear Fusion*, vol. 45, no. 11, p. 1224, 2005.

[11] M. Henderson, R. Heidinger, D. Strauss, R. Bertizzolo, A. Bruschi, R. Chavan, E. Ciattaglia, S. Cirant, A. Collazos, I. Danilov, *et al. Nuclear fusion*, vol. 48, no. 5, p. 054013, 2008.

[12] O. Chellai, S. Alberti, I. Furno, T. Goodman, A. Koehn, L. Figini, D. Ricci, K. Hizanidis, P. Papagiannis, C. Tsironis, and T. team *EPJ Web Conf.*, vol. **03008**, p. 03008, 2017.

[13] J.-M. Moret, B. Duval, H. Le, S. Coda, F. Felici, and H. Reimerdes *Fusion Engineering and Design*, vol. 91, pp. 1–15, 2015.

[14] J. Hawke, Y. Andrebe, R. Bertizzolo, P. Blanchard, R. Chavan, J. Decker, B. Duval, P. Lavanchy, X. Llobet, B. Marlétaz, *et al. Journal of Instrumentation*, vol. 12, no. 12, p. C12005, 2017.

[15] O. Février, C. Theiler, H. De Oliveira, B. Labit, N. Fedorczak, and A. Baillod *Review of Scientific Instruments*, vol. 89, no. 5, p. 053502, 2018.

[16] R. Prater *et al. Nucl. Fusion*, vol. **48**, p. 035006, 2008.

[17] D. Farina *Fusion Sci. Technology*, vol. **52**, pp. 154–160, 2007.

[18] H. Weber, O. Maj, and E. Poli in *EPJ Web of Conferences*, vol. 87, p. 01002, EDP Sciences, 2015.

[19] A. Balakin, M. Balakina, and E. Westerhof *Nuclear Fusion*, vol. 48, no. 6, p. 065003, 2008.

[20] *COMSOL RF Module User's Guide v5.2a.*

[21] O. Chellaï, S. Alberti, M. Baquero-Ruiz, I. Furno, T. Goodman, F. Manke, G. Plyushchev, L. Guidi, A. Koehn, O. Maj, *et al. Phys. Rev. Letters*, vol. 120, no. 10, p. 105001, 2018.

[22] M. Bornatici, R. Cano, O. De Barbieri, and F. Engelmann *Nucl. Fusion*, vol. **23**, p. 1153, 1983.

[23] T. H. Stix, "The theory of plasma waves," *The Theory of Plasma Waves, New York: McGraw-Hill*, 1962.

[24] F. C. Karal Jr and J. B. Keller *Journal of Mathematical Physics*, vol. 5, no. 4, pp. 537–547, 1964.

[25] S. W. McDonald *Physical Review A*, vol. 43, no. 8, p. 4484, 1991.

[26] P. Ricci, F. Halpern, S. Jolliet, J. Loizu, A. Mosetto, A. Fasoli, I. Furno, and C. Theiler *Plasma Physics and Controlled Fusion*, vol. 54, no. 12, p. 124047, 2012.

[27] F. Halpern, P. Ricci, S. Jolliet, J. Loizu, J. Morales, A. Mosetto, F. Musil, F. Riva, T.-M. Tran, and C. Wersal, "The gbs code for tokamak scrape-off layer simulations," *Journal of Computational Physics*, vol. 315, pp. 388–408, 2016.

[28] F. Nespoli, I. Furno, B. Labit, P. Ricci, F. Avino, F. Halpern, F. Musil, and F. Riva *Plasma Physics and Controlled Fusion*, vol. 59, no. 5, p. 055009, 2017.

[29] F. Riva, N. Vianello, M. Spolaore, P. Ricci, R. Cavazzana, L. Marrelli, and S. Spagnolo *Physics of Plasmas*, vol. 25, no. 2, p. 022305, 2018.

[30] F. Riva, E. Lanti, S. Jolliet, and P. Ricci *Plasma Physics and Controlled Fusion*, vol. 59, no. 3, p. 035001, 2017.

[31] F. Riva, "Verification and validation procedures with applications to plasma-edge turbulence simulations," EPFL PhD thesis 2017.

[32] J. S. Bendat and A. G. Piersol *Measurement Science and Technology*, vol. 11, no. 12, p. 1825, 2000.

[33] S. Ahn and J. A. Fessler *EECS Department, The University of Michigan*, pp. 1–2, 2003.

[34] R. A. Fisher *et al. Metron*, 1921.

[35] I. Furno *et al. Phys. Plasmas*, vol. **15**, p. 055903, 2008.

[36] A. e. a. Koehn in *20th Joint Workshop on ECE and ECRH*, (Greifswald), 2018. to appear on EPJ Web of Conferences.